Tooth flank fracture - An applied fatigue study of case hardened bevel gears

Stephan André Böhme[a], Gabor Szanti[b], Joni Keski-Rahkonen[c], Tami Komssi[b], José Garcia Santaella[d], and Alexei Vinogradov[a]*

[a] Norwegian University of Science and Technology (NTNU), Department of Mechanical and Industrial Engineering, Trondheim 7491, Norway
[b] ATA Gears Oy, Tampere FI-33101, Finland
[c] Kongsberg Maritime Finland Oy, Rauma FI-26100, Finland
[d] Tampere University, Faculty of Engineering and Natural Science, Tampere FI-33014, Finland

Abstract

A material model for carburized CrNiMo steel and an advanced shear stress intensity, multiaxial fatigue criterion against surface and subsurface fatigue in bevel gears have been developed and presented in earlier publications. This study assesses the accuracy of the proposed methodology by comparing it to load-controlled bevel gear tests at varying hardening layer thicknesses. The dominant failure mode was wheel-initiated tooth flank fracture. Fractographic analysis by means of scanning electron microscopy revealed a severely elongated $MgO\text{-}Al_2O_3$ cluster in the only pinion-initiated tooth flank fracture. By correlating the calculated material utilizations and the number of cycles to failure, a reiterated lifetime factor is presented. The refined methodology is shown to be capable to differentiate between and accurately predict pitting and subsurface fatigue under well-defined test conditions.

Keywords: Subsurface fatigue, gear testing, rolling contact fatigue, carburized steel

[*] Corresponding author. Tel.: +47 94875749
E-mail address: stephan.a.bohme@ntnu.no

Nomenclature			
varea	Square root of the projected area of an inclusion	NFR	Norwegian research council
a_{BO}, b_{BO}, c_{BO} and d_{BO}	Model parameters BO criterion	p_H	Surface pressure
A	Elongation	P	Power
b	Tooth width	P1	Surface perpendicular path through global $D_{BO,max}$
b_H	Half Hertzian contact width	P2	Path through $D_{BO,max}$ for each depth
BECAL	Bevel Gear Calculation	PIN	Papuga integral multiaxial fatigue criterion
BO	Böhme multiaxial fatigue criterion	R_m	Ultimate tensile strength
CHD	Case hardening depth	R_{p02}	Yield strength
d_e	Outer diameter	R_z	Surface roughness
EBSD	Electron backscatter diffraction	$s_{n,i}$	Chordal tooth thickness for node i
EDS	Energy dispersive X-ray	$s_{n\alpha,i}$	Half tooth thickness for node i
D_{BO}	Material utilization BO criterion	SEM	Scanning electron microscopy
DNV GL	Det Norske Veritas Germanische Lloyd	SN	stress amplitude versus number of load cycles
f_{-1}, f_0	Fatigue limit under fully reversed and repeated axial loading	t_{-1}, t_0	Shear fatigue limit under torsional fully reversed and repeated loading
$f_{-1,K}$	Modified fatigue strength under fully reversed axial loading	T	Oil temperature
f_{xK}	Conversion factor	TFF	Tooth flank fracture
FKM	Forschungskuratorium Maschinenbau	VHCF	Very high cycle fatigue
FZG	Forschungsgesellschaft für Zahnräder und Getriebe	x_{hm}	Profile shift
HV_c	Core hardness	x_{sm}	Tooth thickness factor
HV_i	Hardness in node i	y_{HVmax}	Depth of the hardness peak
HV_s	Surface hardness	y_I	Distance between surface and subsurface nodes
i	Subsurface node	z	Number of teeth
ISF	Isotropic superfinishing	Z	Area reduction
ISO	International Organization for Standardization	Z_{NT}, Y_{NT}	Pitting and tooth root breakage lifetime factors
k_{ap}, k_{fp}	Addendum & dedendum factor	α	Pressure angle
K_{NT}	Lifetime factor	β_m	Mean spiral angle
K_X	Size factor	ϑ, ϕ	spherical angles
LZ	Liu & Zenner multiaxial fatigue criterion	κ	Fatigue ratio
LTCA	Loaded tooth contact analysis	μ	Friction coefficient
m_0	Cutter module	ρ_0	Cutter radius
m_{mn}	Mean normal module	ρ_{eq}	Equivalent radius of curvature
n	Surface node	σ_{nm}, σ_{na}	Normal mean and amplitude stresses
n_1	Pinion RPM	σ_{res}	Residual stress
M_k	Adjusted mean stress sensitivity	τ_m, τ_a	Shear mean and amplitude stresses
MLM	Maximum Likelihood Method		

1. Introduction

Gears, along with the majority of industrial applications, fail predominantly from fatigue. For case hardened cylindrical or bevel gears, typical fatigue failure modes are pitting, tooth root breakage and subsurface fatigue or tooth flank fracture (TFF). Whereas accurate guidelines have been developed for pitting and tooth-root breakage [1, 2], ambiguity surrounds TFF as no clear gear rating standard has yet emerged. This research focuses on subsurface fatigue, the dominant failure mode in large marine bevel gears. Earlier publications [3-5] cover a simplified subsurface fatigue criterion, a material model for carburized CrNiMo steel, a 2D numerical plane strain model and a novel, shear stress intensity, multiaxial fatigue criterion (herein referred to as BO). The BO criterion was developed specifically for fatigue predictions under Hertzian stresses. Based on initial evaluations [5], the proposed methodology is able to differentiate between and accurately predict TFF, pitting and tooth root breakages, extending its applicability from the originally targeted subsurface layer across the entire gear tooth. This article compares the BO criterion against a series of load-controlled bevel gear tests at varying hardening layer thicknesses.

The DNV GL gear rating standard for marine applications [6] features one of the few formalized methods for the prediction of subsurface fatigue. It compares the surface parallel orthogonal shear stress amplitude in the tooth interior with a hardness-derived shear strength. Especially on large gear wheels, where surface hardnesses are typically 1-2 HRC below corresponding pinion values [3], this approach leads to an overestimation of surface rather than subsurface failures. Combining the compressive residual stresses, a result of the case hardening process with the orthogonal shear stress amplitude in the form of a simplified Dang Van criterion leads to an elegant and improved subsurface fatigue prediction [3]. A more accurate fatigue assessment, able to differentiate between pitting failures, tooth root breakages and subsurface fatigue, is possible with the proposed BO shear stress intensity criterion [5]. In a multiaxial fatigue study, comparing the results of different stress-based criteria against test results of steels under static axial, tensile or compressive stresses and oscillating shear stresses, the BO criterion performed on par with the well-established Liu & Zenner (LZ) [7] and Papuga integral method (PIN) [8]. Further merit is given to the BO criterion in a recent study [9] under a wider range of in-phase and out-of-phase loading conditions. Whereas the LZ and PIN criteria work very well under conventional loads [5, 9], they under- or overestimate the likelihood of surface failures under Hertzian stresses. Especially the overestimation of surface failure on gears under large Hertzian stresses is a common issue for a range of stress-based, multiaxial fatigue criteria. In contrast, the BO criterion was specifically developed with large Hertzian stresses in mind.

Highly loaded gears are typically case hardened, resulting in considerable static residual stresses and varying material properties throughout the hardened layer. The developed material model for CrNiMo steels [4] attempts to capture those changes. It is based on high and very high cycle fatigue (VHCF) testing of hourglass-shaped specimen under uniaxial and shear stresses. The specimens were extracted among others, from large 18CrNiMo7-6 and 34CrNiMo6 forgings that underwent gear-like production processes. Testing was done under alternating and oscillating loads. The material properties in the soft core and hard case were captured by the different carbon content and hardness of the forgings. Inferior fatigue properties under uniaxial loading were derived for the approximately 150 HV harder 34CrNiMo6 steel beyond $1 \cdot 10^6$ load cycles. Comparable results between both steels were achieved under shear loading. Scanning electron microscopy revealed similar-sized $MgO\text{-}Al_2O_3$ inclusions in the crack initiation sites for both steels and initiation from large austenite grains for some of the 34CrNiMo6 specimen. The results highlight the criticality of non-metallic inclusions on the uniaxial fatigue strength of hard steels, and the changing fatigue ratio κ. As gears are subjected to large compressive mean normal stresses in the case, and tensile stresses in the core (tensile residual stresses), the changing mean stress sensitivity throughout the hardened layer is critical for an accurate fatigue prediction. A novel approach, relying on the apparent notch effect of non-metallic inclusions on the mean stress sensitivity was proposed [4]. It captures a linearly increasing mean stress sensitivity for soft and mild steels as per the FKM Richtlinie [10] and reduces the trend for hard steels, bridging the gap between the FKM and the model predictions by Murakami [11].

The combination of the proposed multiaxial fatigue criterion [5] alongside the stress and strength models have been shown to capture pitting, tooth root breakage and subsurface fatigue failures in both small and large gears. As the actual load history and precise stress distribution were unknown for the examined gear sets, this study pares the BO criterion with load-controlled bevel gear tests at varying hardening layer thicknesses.

2. Experimental

2.1. *Material and heat treatment*

The test gears were designed and loaded to promote TFF over other fatigue failure modes and to evaluate the effect of the load and the case hardening depth (*CHD*). All pinions were produced from a single melt and a hot rolled 160 mm bar. All wheels were manufactured from a single melt and a 457 mm round forged bar. The materials' chemical compositions, the forging reduction ratios, tensile properties, impact works, degree of purity and heat treatment protocols are listed in Table 1, Table 2 and Table 3. The information given in Table 1 and Table 2 is based on the steel's material certificates and valid for the quenched and tempered condition of the steel prior to case hardening. The tensile properties were determined on 30 mm round bars according to the ISO 6892-1, the impact properties according to the ISO 148-1 and the microinclusions according to the ISO 4967 Method A.

Table 1
Chemical composition and forging reduction ratio of pinion and wheel bars

Steel melt 18CrNiMo7-6	Reduction ratio	Composition (wt. %)										
		C	Mn	P	S	Si	Ni	Cr	Mo	Cu	Al	O
Pinion	6:1	0.17	0.62	0.007	0.002	0.30	1.60	1.65	0.31	0.22	0.031	0.0011
Wheel	5.1:1	0.16	0.53	0.005	0.001	0.26	1.59	1.68	0.29	0.11	0.035	0.0012

Table 2
Tensile properties, impact work and degree of purity of pinion and wheel bars

Tensile properties	Yield strength	Ultimate strength	Elongation	Area reduction	Impact Work [J]	Degree of purity [ISO4967-A]			
[ISO 6892-1]	R_{p02} [MPa]	R_m [MPa]	A [%]	Z [%]	[ISO 148-1]	A	B	C	D
Pinion	1144	1436	11.1	49	66/72/73	0.5/0.5	1/0	0/0	1/0.5
Wheel	938	1243	12	56	77/76/68	0/0	1/0.5	0.3/0.3	1/0.5

Table 3
B1-B3 test gear batches with number of produced gears sets, heat treatment parameters and average hardness results

Heat treatment batches	No. of gear sets	Carburizing durations [h]	$HV_{S1,2}$ [HRC]	$HV_{C1,2}$ [HV]	$CHD_{1,2}$ [mm]
B1	3	36	60/59	430/400	2.5/2.1
B2	1	40	60/59	430/400	2.6/2.4
B3	6	50	61/60	455/425	3.0/2.9

The case hardening process consisted of carburizing, direct quenching in oil and a 5 hour tempering at 170 °C. For the B3 gears, a more effective quenching media was used, resulting in slightly elevated surface and core hardness (see Table 3). The large differences in the obtained *CHDs* between the pinions and wheels of batch B1 are due to the increased stock removal on the wheels during hard cutting. The heat treatment of the B1 gears was performed with inadequate clamping, resulting in excessive thermal deflections and thus stock removal on the wheels during

hard cutting. HV10 hardness measurements were carried out on multiple pinion and wheel teeth of each gear set after failure. For a minimum of one gear set per heat treatment batch, multiple hardness profiles were obtained along the tooth flank to capture the occurring hardness transition from the tooth root to the tip. Fig. 1 exemplifies the results of the performed hardness measurements on gear set B3-2. Clearly visible are the increasing hardening layer thickness, core and surface hardness from root to tip on the plotted wheel tooth.

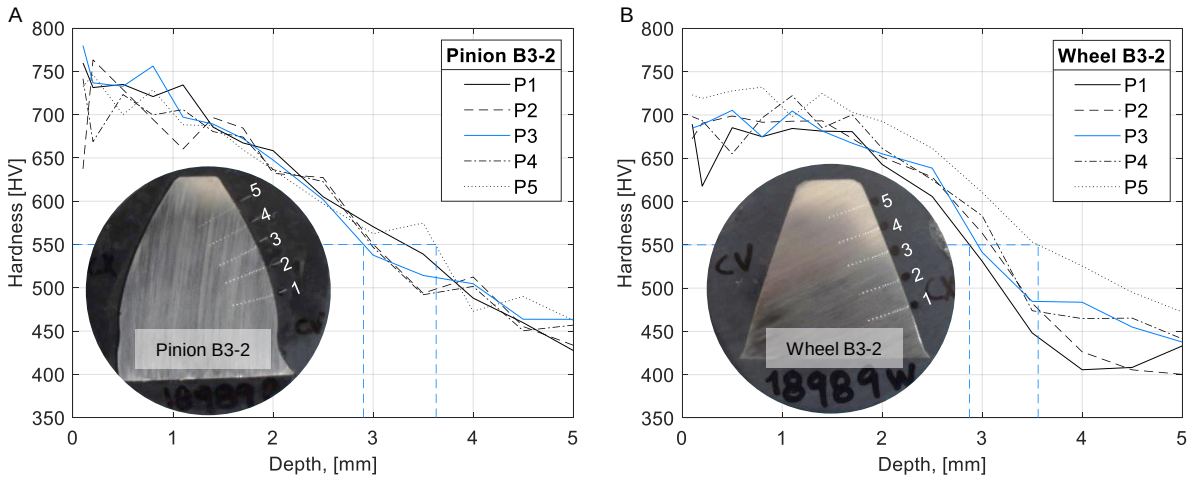

Fig. 1. Hardness measurements and hardness map of (A) pinion gear tooth on B3-2 and (B) wheel gear tooth B3-2

The measurements were used to create a model of the hardness distribution of the entire gear tooth [5]. Three sets of hardness parameters according to the Thomas model [12] (one for the tooth root, one for the pitch line and a third for the tooth tip) were used to describe the hardness transition in tooth profile direction. As shown in Fig. 1, the hardness profiles on the B3-2 pinion tooth were very uniform, whereas the wheel hardness profiles changed significantly from root to tip. Visible is also a steeper hardness transition from case to core on the wheel tooth. The Thomas model allows the description of these differences through the parameter y_{HVmax} as the depth of the hardness peak. Rather than using it for its intended purpose, it is set to control the gradient of the hardness profile. For the two blue lines in Fig. 1A and B (representing the measurements taken on the mid tooth height), y_{HVmax} was set to -0.8 mm for the pinion and 0.48 mm for the wheel. In the gear endurance tests, TFF initiated predominately on the wheels, despite the 9:33 gear ratio and the larger number of load cycles on the tested pinions. With TFF typically initiating in a depth corresponding to 1-2x the *CHD*, the above-outlined hardness differences must be regarded as a contributing factor.

2.2. *Gear specimen*

Table 4 summarizes the test gears' macro geometry, the measured surface roughnesses and case hardening depths for pinions and wheels. The chosen gear geometry, the use of a high viscosity ISO-VG 220 gear oil and polishing of the gears through isotropic superfinishing (ISF) were implemented to ensure TFF over pitting, tooth root breakage or scuffing failures even at extreme surface pressures (> 2000 MPa).

Table 4
Macro geometry, measured roughness and hardness on tests gears B1-B3

Description	Unit	Macro Geometry Pinion	Wheel	Gear	$R_{z1,2}$ [µm]	$CHD_{1,2}$ [mm]
Pressure angle, α	°	20		B1-1	0.6/0.4	2.5/2.2
Number of teeth, z	-	9	33	B1-2	1.2/0.6	2.4/2.0
Outer pitch diameter, d_e	mm	122.7	450	B1-3	1.0/0.7	2.5/2.1
Tooth width, b	mm	82		B2-1	0.6/0.4	2.6/2.4

Mean spiral angle, β_m	°	32.8		B3-1	0.4/0.2	2.9/3.0
Profile shift, x_{hm}	-	0.35	-0.35	B3-2	0.4/0.2	3.0/3.0
Tooth thickness factor, x_{sm}	-	0.01	-0.03	B3-3	0.4/0.3	2.9/2.9
Adddendum/Dedendum factor, k_{ap}/k_{fp}	-	1.05/1.3125		B3-4	0.4/0.2	2.8/3.0
Cutter module, m_0	mm	10		B3-5	0.5/0.5	2.9/2.9
Cutter radius, ρ_0	mm	170		B3-6	0.4/0.2	2.9/2.9

All test gears featured an identical macro and micro geometry that varied only due to individual machining deviations. In order to capture the resulting surface stresses between meshing pinion and wheel teeth, the actual tooth geometries were obtained by gridded coordinate measurements and used as a point cloud to model the tooth flank. The load dependent gear deflections were estimated through finite element simulations, considering the gear and its environment. To estimate the friction coefficients between the contacting flanks, oil temperature and surface roughness measurements were carried out on each gear set. The average operating temperatures ranged from 33 to 36 °C and the surface roughnesses of the ISF treated teeth from R_z 0.2 to 1.2 µm.

2.3. *Test machine and procedure*

The tests were carried out on a back-to-back bevel gear test rig. It operates in a mechanical power circuit, meaning that after a static load has been applied, only the internal friction needs to be overcome during operation (see Fig. 2A). The principle is similar to the well-established FZG cylindrical and bevel gear test rigs but uses a hydraulic torque actuator rather than a preloading clutch for the application of load. It pairs two test gears working with two, larger, failure-free transmission gears. Compared to the FZG's bevel and hypoid test rigs, significantly larger gears can be tested with a wheel outer pitch diameter of 450 mm rather than 170 mm, making these test results more transferable to large industrial applications like bevel gears in azimuthing thrusters.

A B

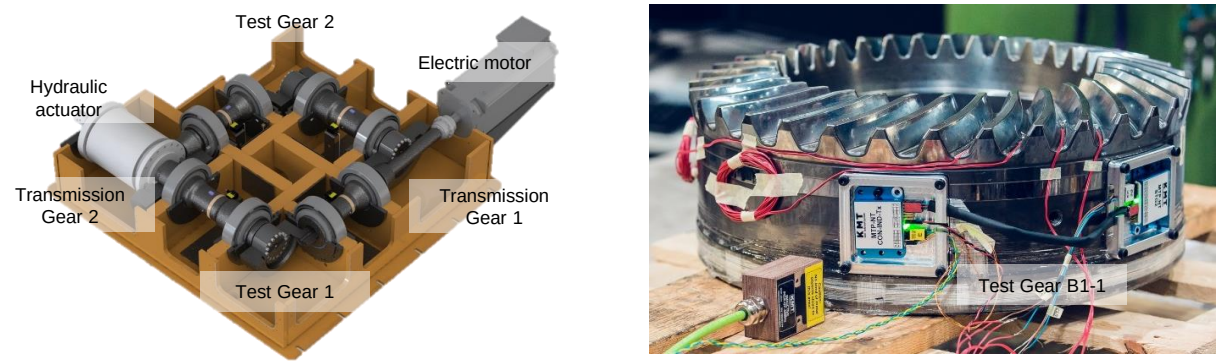

Fig. 2. (A) Schematics of the bevel gear test rig with two test gears and two larger transmission gears and (B) telemetry set-up on test gear B1-1

Each axle between the test rig's corners was equipped with a strain gauge and telemetry system to document the transmitted torque, frictional losses and internal dynamics. Between the two test corners, mechanical losses of approximately 50 kW were measured, reducing the surface pressure on the gears tested in corner 2 by roughly 25 MPa. The contact stress analysis showed that the reduction in surface pressure due to frictional losses was in some cases compensated by occurring machining deviations (see Table 5). Unique to gear set B1-1 was a strain gauge and telemetry set-up, by which the bending stresses on 2 wheel teeth could be measured directly during operation (see Fig. 2B).

Endurance testing was done at 1500 RPM and at uniform loads at 750, 875 and 1000 kW. Torque during testing was

controlled by the hydraulic actuator based on the torque measurements on the machine axes. Each gear underwent a run-in procedure with a gradual load increase (typically less than 1 % of the total test duration). Gears were only replaced after failure or once the run-out limit of $5 \cdot 10^7$ load cycles on the pinion had been achieved. As the set-up required two test gears to be run simultaneously, individual gears were occasionally tested at multiple load levels. An equivalent load was calculated for each gear based on the measured load history using the ISO6336-6 guideline [13]. The specified loads in Table 5 describe, therefore, the friction-corrected, equivalent loads for each gear.

Table 5
Load parameters for all test gears, including RPM, equivalent power, maximum surface pressure, average oil temperature and max friction coefficient

Description		Gears									
	Unit	B1-1	B1-2	B1-3	B2-1	B3-1	B3-2	B3-3	B3-4	B3-5	B3-6
Pinion RPM, n_1	1/min	1500 (for all test gears)									
Power, P	kW	814	859	999	1000	990	1000	800	1050	793	847
Max surface pressure, p_{Hmax}	MPa	1938	1937	2031	2012	2012	2038	1943	2076	1901	1953
Average oil temperature, T	°C	35	33	34	33	36	35	36	35	36	36
Max friction coefficient, μ_{max}	-	0.050	0.053	0.054	0.051	0.048	0.048	0.047	0.048	0.049	0.047

The gears' surface stresses, a result of the applied load, the actual macro- and microgeometry and the load-dependent gear deflections, were modelled through a loaded tooth contact analysis (LTCA with BECAL 5.0 [14]). BECAL is a software developed by the Institute of Machine Elements and Machine Design at the Dresden University of Technology. A spiral bevel gear's tooth geometry cannot be modelled analytically and relies in the case of BECAL on a machining simulation. In order to consider the pitch error and gear deflections alongside the gear's macro- and microgeometry, a no-load contact analysis is initially run, defining the distance between opposing flank points for a discrete number of contact positions. The resulting global ease-off is then used in the loaded tooth contact analysis that predicts the stresses between the meshing gear flanks. As a result of the segmentation of the gear tooth in lengthwise and tooth profile directions, influence coefficients are calculated that capture the interaction between the segments, allowing for a short computing time and high precision.
Resulting stress distributions are plotted in Fig. 3 for the gear flank and mean cross-section of the B1-1, B1-2, B3-1 and B3-2 pinions. As is typical for crowned bevel gears, the highest surface stresses occur in the middle of the tooth, deeming the analysis of the gear's mean cross-section sufficient for the evaluation of surface and subsurface failures.

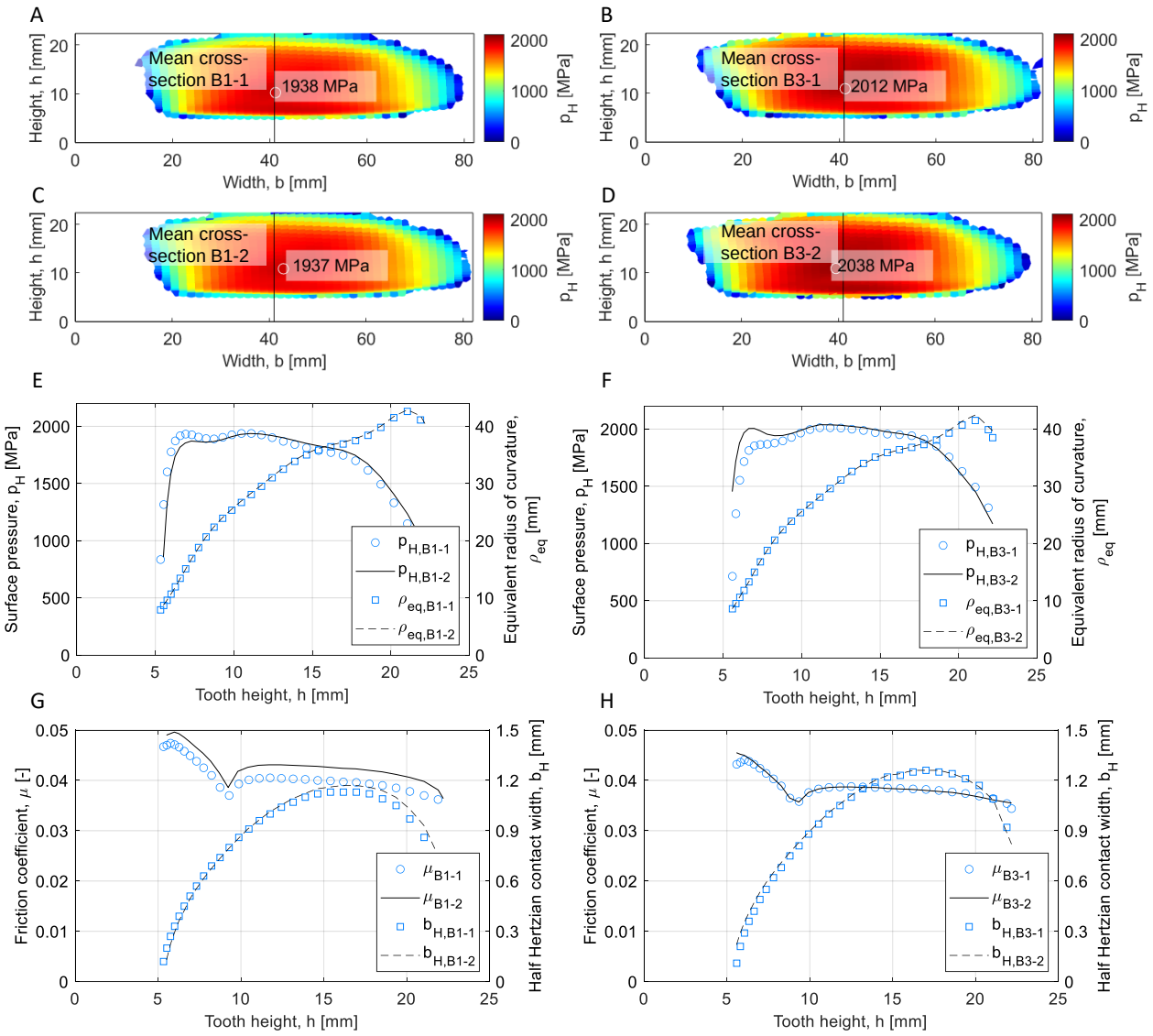

Fig. 3. Prediction of the surface pressure p_H for contact patterns B1-1 in (A), B3-1 in (B), B1-2 in (C) and B3-2 in (D). Comparison of the surface pressure p_H and equivalent radius of curvature ρ_{eq} in the gears' mean cross-section between B1-1 and B1-2 in (E) and B3-1 and B3-2 in (F). Comparison of local friction coefficient μ and half Hertzian contact width b_H in the gears' mean cross-section between B1-1 and B1-2 in (G) and B3-1 and B3-2 in (H).

Fig. 3 highlights the correlation between the applied load, the surface pressure and the contact length, but also the effect of the machining deviations. In Fig. 3 A and C, the contact stress distributions for gears B1-1 and B1-2 are shown. These gears were tested together in corners 1 and 2 of the test rig and subjected to an equivalent load of 814 and 859 kW, resulting, despite the 45 kW load difference, in nearly identical contact patterns and stress distributions. Fig. 3 B and D plot the contact stress distributions for gears B3-1 and B3-2. Both were tested at approximately 1000 kW, resulting in 100 MPa higher surface pressure and a 4 mm wider contact pattern compared to B1-1 and B1-2. Beyond the surface pressure, the equivalent radius of curvature ρ_{eq}, friction coefficient μ and half Hertzian contact width b_H for the mean cross-sections of the 4 gears are also plotted in Fig. 3 E, F, G and H. Nearly identical ρ_{eq} values are reported for all test gears, underlining the machining accuracy and geometrical comparability of all gears. Subplots G and H in Fig. 3 highlight the subtle differences in the friction coefficient μ as a result of the varying surface roughnesses between the gears. The friction coefficient was predicted according to Hombauer [15], relying on the works by Klein [16] and Wech [17]. With pure rolling only being present in the gear's

pitch point, the plotted friction coefficients are minimal at around 9 mm tooth height and increase towards the gear's root and tip. The last parameter included in Fig. 3 G and H is the half Hertzian contact width b_H. For a cylinder/plane contact model, it critically affects the depth of the acting shear stresses inside the material.

3. Simulation

The calculation of the material utilization D_{BO}, defined as the inverse of the local safety factor against fatigue, is briefly introduced in this section [5]. All inputs needed for the prediction of D_{BO} are given in the previous sections (i.e. the gear geometry, the load, surface roughness and hardness parameters).
The approach relies on the stress analysis in the gear's mean cross-section and the 2D plane strain simplification. This is deemed appropriate due to the stress concentration in the middle of the tooth for crowned bevel gears (see Fig. 3) and the documented minimal subsurface stress differences between the 2D and 3D analysis [18, 19]. As such, a seminumerical approach is pursued, avoiding the need for the finite element contact analysis. In the first step, the mean cross-section of the bevel gear's virtual cylindrical gear is modelled, meshed, and loaded with the LTCA derived stress profile. Herein an improved machining simulation was implemented [5] to capture the tooth root's trochoidal shape. Fig. 4 visualizes the machining simulation and the subsequent mesh generation with a coarse 0.3 mm element size to visualize the mesh layout. For the actual calculations, a finer 0.1 mm element size with 'T6' triangular elements was used. For these quadratic triangular elements, a full integration over three Gaussian integration points was implemented. All surface nodes below the gear's tooth root diameter had a fixed constraint applied to them, and all surface nodes underneath an instantaneous contact position (defined by its position along the tooth profile, its half Hertzian contact width b_H and surface pressure p_H) were loaded according to their specific Hertzian stress distribution. For the pinion tooth plotted in Fig. 4 and the implemented 0.1 mm mesh resolution, 144 contact positions with non-zero contact stresses were analyzed.

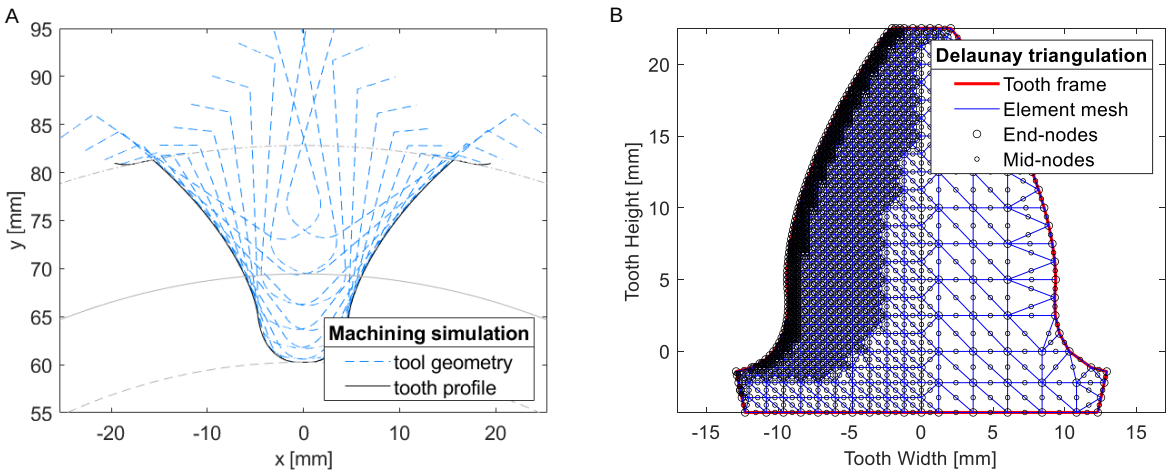

Fig. 4. (A) B1-1 virtual pinion tooth machining simulation and (B) mesh layout

As is shown in Fig. 4B, the element size is doubled after 1/16 and 1/3 of the mean normal circular tooth width s_{mn} as well as in the middle of the gear tooth. This stepped mesh ensures a load introduction of the Hertzian stress profile in each contact position over a large number of nodes and an efficient calculation.
The hardness and residual stress model remained unchanged [5]. Each surface node *n* is assigned a set of hardness parameters according to the Thomas model [12] and its position in the tooth profile direction. The same is done subsequently for each subsurface node *i*, based on its closest surface nodes. For the estimation of the residual stresses, the Lang model [20] is used up to the *CHD*, followed by a 4th order polynomial to describe the tensile residual stresses in the core. Lines 1 and 2 in Eq. 1 are according to Lang with lines 3 and 4 describing the polynomial and the equilibrium constraint, used to derive the constants *a*, *b* and *c* along with the tangential constraint in the transition point (*CHD*).

$$\sigma_{res,i}(y_l) = \begin{cases} -5/4 \cdot \left(HV_i(y_l) - HV_{C,i}\right), & HV_i(y_l) - HV_{C,i} \leq 300 \text{ HV and } y_l < CHD_i \\ 2/7 \cdot \left(HV_i(y_l) - HV_{C,i}\right) - 460, & HV_i(y_l) - HV_{C,i} > 300 \text{ HV and } y_l < CHD_i \\ a \cdot \left(y_l - s_{n\alpha,i}\right)^4 + b \cdot \left(y_l - s_{n\alpha,i}\right)^2 + c, & y_l \geq CHD_i \end{cases} \quad (1)$$

$$\text{with} \quad s_{n\alpha,i} = \frac{s_{n,i}}{2 \cdot \cos \alpha_i} \quad \text{and} \quad \int_0^{s_{n\alpha,i}} \sigma_{res,i}(y_l)\, dy_l = 0$$

The index *i* in Eq. 1 refers to each subsurface node with its assigned core hardness $HV_{C,i}$ and local hardness $HV_i(y_l)$. The variable y_l describes the perpendicular path from the closest surface node through studied subsurface node *i* to the middle of the tooth (here described through the half tooth thickness $s_{n\alpha,i}$). Each node's local hardness along with an assumed global inclusions size (set through Murakami's √area parameter ≈ 80 µm [4]), the fatigue ratio κ and an adjusted mean stress sensitivity M_k, are used to define the local fatigue parameters throughout the gear tooth. They are set according to the material model for CrNiMo steel [4].

$$f_{-1}(HV) = \begin{cases} 1.6\, HV, & HV < 300 \\ \dfrac{1.56 \cdot (HV + 120)}{\left(\sqrt{area}\right)^{\frac{1}{6}}}, & HV > 550 \\ 505 \text{ MPa}, & \text{else} \end{cases} \quad \text{and} \quad f_0 = \frac{2 \cdot f_{-1}}{1 + M_k} \quad (2)$$

$$t_{-1} = \frac{f_{-1}}{\kappa} \quad \text{with} \quad \kappa = -5 \cdot 10^{-4}\, HV + \sqrt{3} \quad \text{and} \quad \frac{4t_{-1}}{t_0} - \frac{2f_{-1}}{f_0} = 1$$

In Eq. 2 f_{-1}, f_0, t_{-1}, t_0 describe the fatigue limit under fully reversed and repeated axial loading and torsional fully reversed and repeated loading (t_0 according to Liu and Zenner [7]) at $2 \cdot 10^6$ load cycles. These fatigue limits are subsequently used to determine the model parameters in the multiaxial fatigue criterion in order to combine the different stress components to an equivalent stress. For the prediction of the local material utilization D_{BO}, the equivalent stress is compared against a modified fatigue strength under fully reversed axial loading $f_{-1,K}$. The modifications include a load cycle dependency, size effect and failure probability conversion. The lifetime factor K_{NT} relied in its first iteration on the high cycle and very high cycle uniaxial fatigue results of the 34CrNiMo6 steel [4]. It is reiterated in this study through the analysis of the gear test results with the Maximum Likelihood Method (MLM) [21] and therefore omitted from Eq. 3. The size factor K_X listed in Eq. 3 describes a simplification of the weakest link theory [22], relying on the comparison of the highly stressed volume in the fatigue specimen and the studied gear sets [4, 5]. In its simplified form, it depends on the gear's mean normal module m_{mn} and is identical to the ISO suggested size factor for the tooth root [2]. As such, K_X ignores the differences between the tested pinions and wheels and the effect of the applied load on the highly stressed volume. The calculations in this study rely therefore directly on the weakest link theory and not the outlined equation. For gear standards [1, 2, 6], the endurance limit is set for a 1 rather than 50 % failure probability, requiring a conversion factor f_{xK} to convert the gear test results. For the documented standard deviation of 4 % [4], a conversion factor of 0.91 is suggested. The analysis of gear test results and all calculations in this study omit f_{xK}.

$$f_{-1,K} = f_{-1} \cdot f_{xK} K_X K_{NT}$$
$$f_{xK} = 0.91 \quad \text{and} \quad K_X = 1.05 - 0.01 \cdot m_{mn} \quad \text{with} \quad 0.87 \leq K_X \leq 1 \quad (3)$$

Fig. 5A plots the hardness against the residual distribution for a B1-1 pinion tooth and the hardness against the fatigue strength f_{-1} in Fig. 5B.

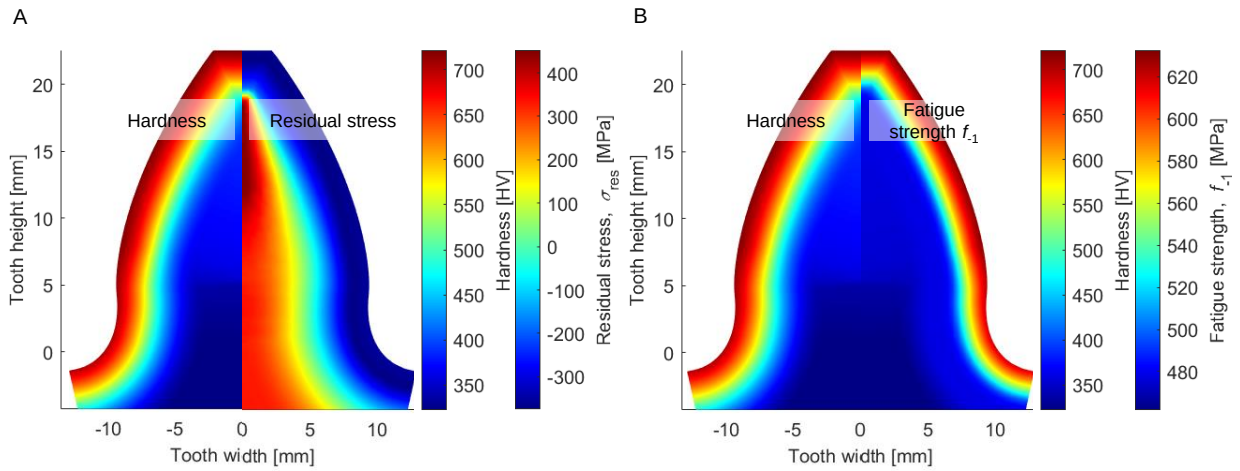

Fig. 5. (A) Hardness and residual stress and (B) uniaxial fatigue strength prediction for a B1-1 pinion tooth for measured hardness parameters *CHD* = [2.2, 2.5, 3.7] mm, HV_s = [703, 718, 720] HV, HV_c = [322, 362, 380] HV in tooth profile positions *h* = [2, 8, 16] mm

In accordance with the performed hardness measurements (see Fig. 1), an increase in surface and core hardness and *CHD* is visible in Fig. 5A in profile direction. Whereas large marine bevel gears are typically produced with a CHD/m_{mn} ratio from 0.12 - 0.21, the test gears' ratio ranged from 0.21 - 0.32, resulting in a wide layer of compressive residual stress and relatively large tensile stresses in the core, increasing towards the narrow tooth tip. The differences in local hardness and fatigue strength f_{-1} are plotted in Fig. 5B. The in Eq. 2 outlined fatigue model [4] describes a transition from the upper to the lower limit of Murakami's fatigue model [11] within the hardness range 300-550 HV. This transition is visible in Fig. 5B as f_{-1} remains nearly constant in the tooth core and only starts to increase in the case, once the local hardness exceeds 550 HV.
The modelled hardness distribution deviates slightly from the measured core hardnesses. This was done intentionally in order to increase the compressive residual stress levels in the surface. The residual stress model by Lang [20] (see Eq. 1) predicts diminishing compressive, residual stress levels for gears with high core hardnesses (see Table 3 and Fig. 1). On case hardened gears, the residual stresses are a result of the martensitic transformation, occurring first in the case/core interface, subsequently in the core and finally on the surface. As such, the resulting residual stresses are a function of the local cooling rate and, predominately, the carbon content. It could therefore be argued that the residual stress should be modelled as a function of the carbon profile and not the hardness.

With the static residual stresses and the material properties defined, a numerical stress calculation is carried out for each contact position and the defined 2D plane strain stress state. The resulting time-dependent stress matrices are combined to normal mean and amplitude stresses (σ_{nm} and σ_{na}) and shear mean and amplitude stresses (τ_m and τ_a) on each material plane, defined by the spherical angles ϑ and ϕ. Whereas the prediction of the normal stresses is straight forward, the maximum rectangular hull method (MRH) was applied to estimate the shear stress components. The predicted stresses are integrated over all material planes to an equivalent stress as per Eq. 4 and compared against the adjusted uniaxial fatigue strength $f_{-1,K}$ (see Eq. 3). Eq. 4 outlines the stress integration and prediction of the model parameters a_{BO}, b_{BO}, c_{BO} and d_{BO} from the fatigue parameters f_{-1}, f_0, t_{-1}, t_0.

$$D_{BO} = \frac{\sqrt{\frac{15}{8\pi}\int_0^{2\pi}\int_0^{\pi}\left((a_{BO}\tau_a^2 + b_{BO}\sigma_{na}^2)(1 + c_{BO}\sigma_{nm})^2 + d_{BO}\tau_a\tau_m\right)\sin(\theta)\,d\theta d\varphi}}{f_{-1,K}} \tag{4}$$

$$a_{BO} = \frac{1}{5}(3\kappa^2 - 4) \text{ and } b_{BO} = \frac{1}{5}(6 - 2\kappa^2)$$

$$c_{BO} = -\frac{3f_0(11-2\kappa^2)}{70C} + \sqrt{\left(\frac{3f_0(11-2\kappa^2)}{70C}\right)^2 + \frac{1}{C}\left(\left(\frac{2f_{-1}}{f_0}\right)^2 - 1 - \frac{\kappa^2}{3}\left(\left(\frac{2t_{-1}}{t_0}\right)^2 - 1\right)\right)}$$

$$d_{BO} = \frac{\kappa^2}{3}\left(\left(\frac{2t_{-1}}{t_0}\right)^2 - 1 - \frac{c^2 t_0^2}{35\kappa^2}(8-\kappa^2)\right) \quad \text{with} \quad C = \frac{f_0^2}{84}(17-4\kappa^2) - \frac{t_0^2}{105}(8-\kappa^2)$$

4. Results & Discussion

4.1. *Fatigue results*

A series of 10 gear sets were endurance tested with their geometry, loads and material properties described in the previous sections of this article. Fig. 6A plots the cycles to failure and run-outs against the corresponding maximum Hertzian contact stress in the mean cross-section. The single pinion-initiated pitting and TFF failures are highlighted. In contrast, Fig. 6B shows the maximum of the material utilization D_{BO} calculated according to Eq. 4 without the lifetime factor K_{NT} and conversion factor f_{xK}.

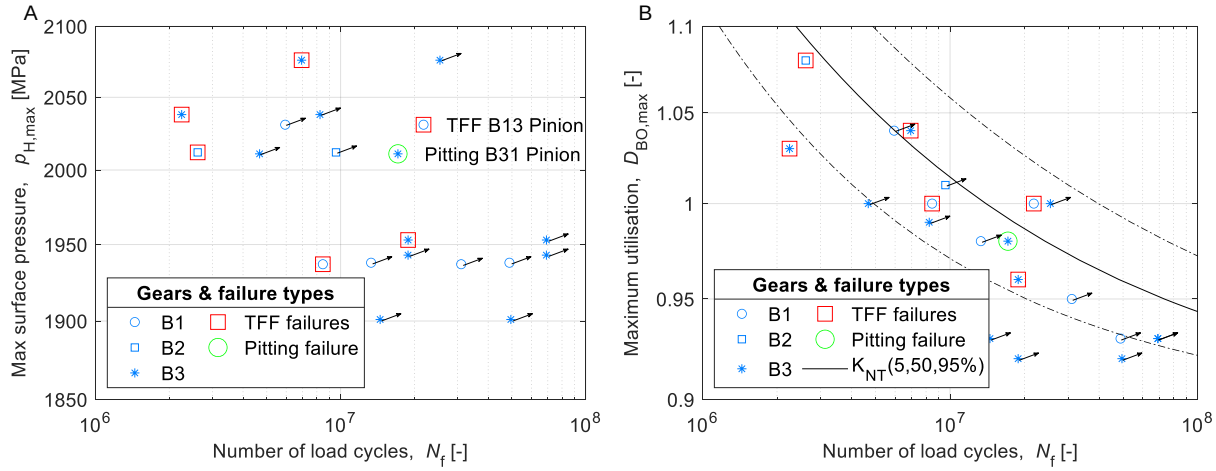

Fig. 6. Gear test results plotted as (A) number of load cycles N_f against maximum surface pressure p_H and (B) number of load cycles N_f against maximum material utilization $D_{BO,max}$

As a result of the hardness variations between and within the heat treatment batches, plotting the number of cycles N_f against the maximum occurring Hertzian contact stress leads to inconclusive results. Of the 7 observed fatigue failures, 5 TFF failures occurred on the wheels of B1-2, B2-1, B3-2, B3-4 and B3-6, 1 TFF failure on the pinion of B1-3 and 1 pitting damage on the pinion of B3-1. The 9:33 gear ratio on the test gears meant that each pinion tooth was subjected a 3.67x larger number load cycles than corresponding wheel teeth, suggesting that a majority of the fatigue failures should have occurred on pinions rather than wheels.

Plotting N_f against the maximum material utilization $D_{BO,max}$ (see Fig. 6B) leads to far more conclusive results as the available data on the stress and strength differences between the tested pinions and wheels is combined. By omitting K_{NT} and f_{xK} from Eq. 3 and 4, a quasi-stress amplitude versus number of load cycles curve (SN-curve) is visualized. The a quasi SN-curve was approximated through the use of the maximum likelihood method [21], combining run-outs with TFF and pitting failures. Fig. 7 compares the lifetime factors of the performed gear endurance tests against the VHCF results of the tested 18CrNiMo7-6 and 34CrNiMo6 steels [4] and against those quoted in the ISO standard for pitting and tooth root breakage [2, 23].

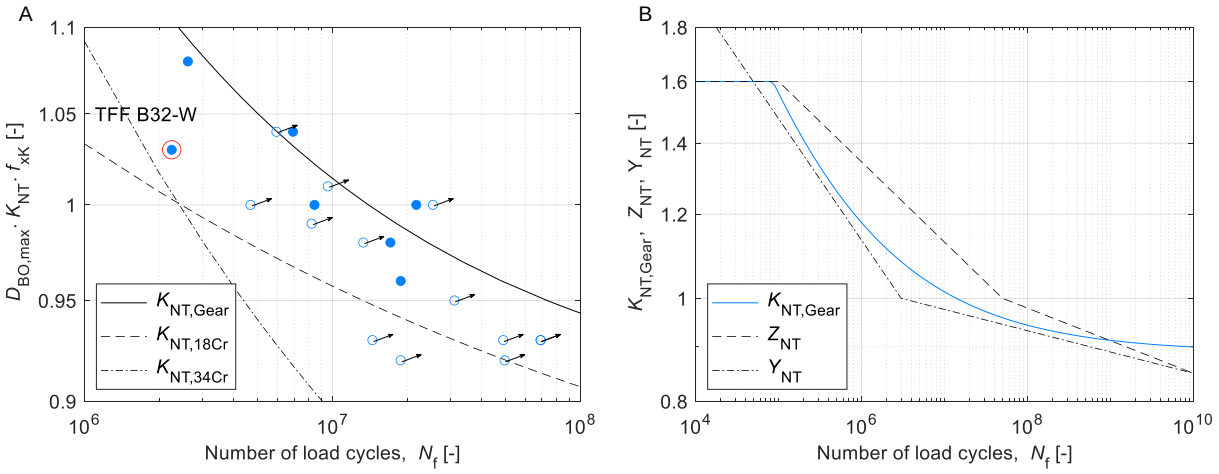

Fig. 7. Comparison between predicted lifetime factor $K_{NT,Gear}$ and (A) reported results for 18CrNiMo7-6 $K_{NT,18Cr}$ and 34CrNiMo6 $K_{NT,34Cr}$ and (B) ISO predictions Z_{NT} and Y_{NT}

At fewer cycles, $K_{NT,Gear}$ shows a pronounced load cycle dependency that diminishes in the VHCF regime. It transitions from a lifecycle factor closer to the tested 34CrNiMo6 steel to the 18CrNiMo7-6 steel [4]. The TFF failure on the wheel of B3-2 after $2.25 \cdot 10^6$ load cycles marked in red in Fig. 7A can be seen as an outlier to the predicted SN-curve. It, along with the TFF failures on the B1-3 pinion tooth and B2-1 wheel tooth were investigated further by means of scanning electron microscopy (SEM). Fig. 7B compares $K_{NT,Gear}$ against the pitting and the tooth root breakage related lifetime factors Z_{NT} and Y_{NT} [1, 2]. Plotted are the ISO factors without permissible pitting damages and with deteriorating fatigue properties in the VHCF regime. The lifetime factor $K_{NT,Gear}$ is capped conservatively at 1.6 based on the reported yield strength to fatigue ratio of the tested 18CrNiMo7-6 steel. Only a limited number of tests were performed with failures and run-outs occurring between $2 \cdot 10^6$ and $7 \cdot 10^7$ load cycles, resulting in a lifetime factor that is sensitive to small deviations in the calculated material utilizations. By relying on material utilization rather than surface stress, the lifetime factor considers the gear size, the applied load and hardening procedure. As such, other gear test results could be added to complement the presented results.

$$K_{NT,Gear} = \exp\left(\frac{\ln(N_f) - 10.42}{-2.73}\right) + 0.89 \quad \text{with} \quad K_{NT,Gear} \leq 1.6 \tag{5}$$

Utilizing the derived lifetime factor as per Eq. 5, the material utilizations for all test gears were recalculated and plotted for gear sets B1-3, B2-1, B3-1 and B3-4 in Fig. 8 and Fig. 9. Failures are expected for gears with material utilizations close to or larger than 1 and no failures for material utilizations significantly smaller than 1. D_{BO} is plotted in Fig. 8 for the gear's mean cross-section and in Fig. 9 for two paths, one perpendicular to the tooth surface through $D_{BO,max}$ (P1 in Fig. 8 and Fig. 9) and a second one intersecting the maximum utilization for a given material depth (P2 in Fig. 8 and Fig. 9). By doing so, the comparison of surface against subsurface fatigue is enabled as pitting, tooth root breakage and TFF are expected to initiate in different positions along the tooth profile.

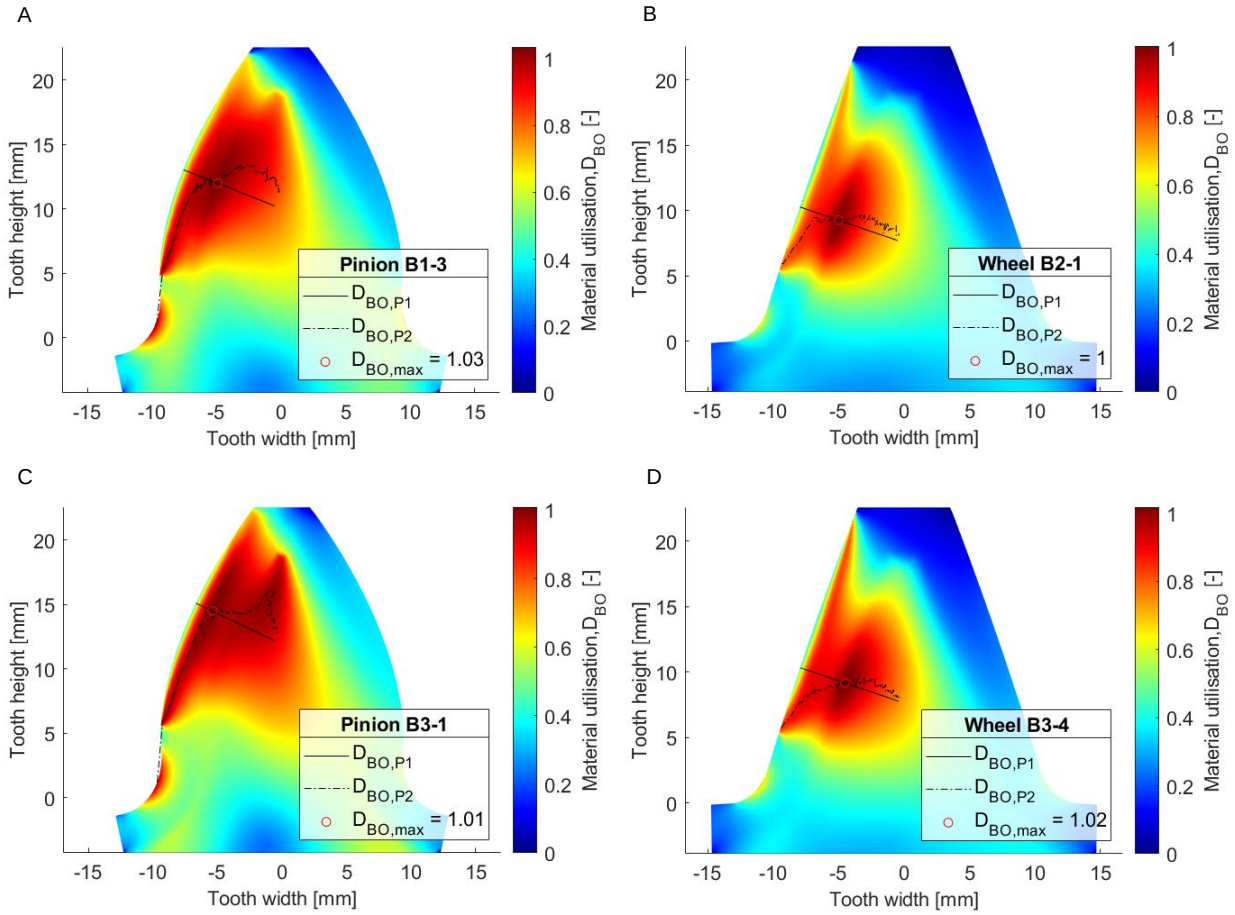

Fig. 8. Material utilizations for mean cross-section of (A) pinion B1-3, (B) wheel B2-1, (C) pinion B3-1 and (D) wheel B3-4

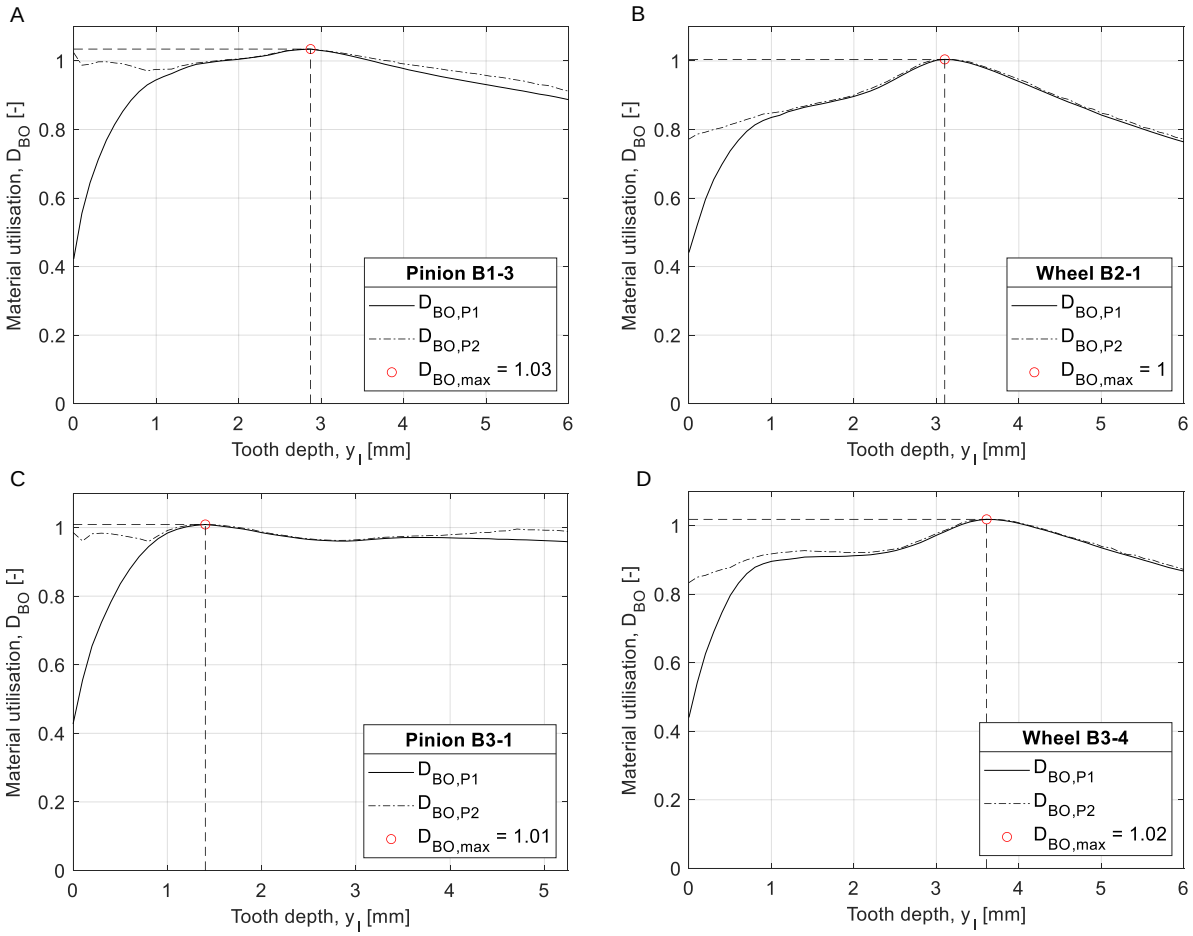

Fig. 9. Material utilization along path 1 & 2 for mean cross-sections of (A) pinion B1-3, (B) wheel B2-1, (C) pinion B3-1 and (D) wheel B3-4

Focusing on Fig. 9B and D, the effect of an increasing *CHD* on the predicted depth of the maximum material utilization can be observed. As listed in Table 4, the case depth of wheel B3-4 was 0.6 mm deeper than for wheel B2-1. Accordingly, the location of the maximum material utilization can be found approximately 0.5 mm deeper on B3-4. Gear set B2-1 with a 2.4 mm *CHD* suffered a TFF damage after $2.61 \cdot 10^6$ load cycles on the wheel, whereas gear set B3-4 with its 3.0 mm *CHD* endured $6.94 \cdot 10^6$ load cycles at a 64 MPa larger surface stress (see Table 5) prior to failure.

Comparing Fig. 9A and B against C and D demonstrates the higher risk for surface fatigue on the tested pinions than wheels. This finding is in good agreement with recent studies on the pitting durability on bevel gear [24], whereby 33.5 % Hertzian contact stresses are allowable on driven rather than driving gear flanks. Fig. 9A plots the predicted material utilization for a B1-3 pinion tooth. As shown in the next section, the calculated utilization peak in a depth of 2.7 mm agrees well with the observed TFF initiation 2.4 mm below the surface. A local utilization peak of 1.01 in a depth of 1.3 mm is predicted for the B3-1 pinion and visualized in Fig. 9C. With pitting damages initiating either directly on the surface or in a shallow depth below the surface, the stress and strength model, along with the multiaxial fatigue criterion are deemed appropriate to predict both pitting and TFF damages. The current iteration of the stress model does not consider elasto-hydrodynamic and surface roughness effects on the Hertzian stress distribution. With those effects, a utilization peak closer to the surface is probable. A third peak on B1-3 and B3-1 pinions in the tooth dedendum and a depth of 0.3 mm may indicate a substantial risk for micropitting on these gears. The peak's location on the tooth profile and its absence on the tested wheels corresponds well with the predictions made by Hombauer [15]. With micropitting damages being currently attributed to local oil film

thicknesses rather than a fatigue stress analysis, no statement in regard to the applicability of the developed methodology in predicting micropitting damages can be made at this stage. Fig. 10 shows the gear failures on gears B1-3, B2-1, B3-1 and B3-4.

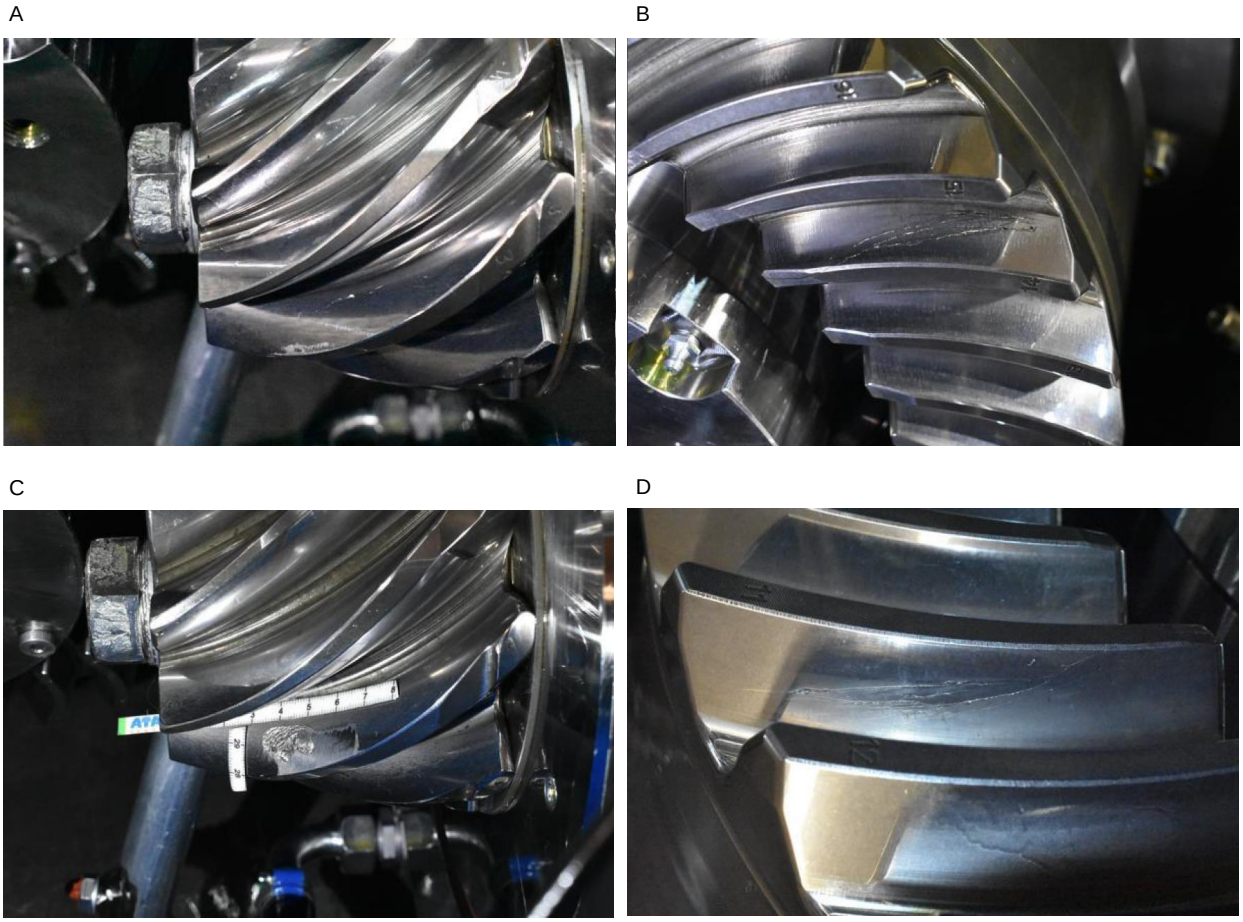

Fig. 10. Gear failures due to subsurface fatigue on (A) pinion B1-3 after $3.1 \cdot 10^7$ load cycles, (B) wheel B2-1 after $2.61 \cdot 10^6$ load cycles and (D) wheel B3-4 after load cycles $6.9 \cdot 10^6$ and pitting on (C) pinion B3-1 after $1.7 \cdot 10^7$ load cycles

Whereas the pitting damage is clearly visible on B3-1, the TFF damages on B1-3, B2-1 and B3-4 are visible as a crack network, stretching across the loaded pinion and wheel flanks. As reported by other researchers [25-27], once the primary subsurface crack transitions from mode II to mode I, multiple secondary cracks form and grow towards the load-carrying flank. The orientation of the crack network at an angle parallel to the instantaneous contact lines between meshing pinion and wheel teeth is also clearly visible. In addition to the above-mentioned, primary TFF and pitting damages, scuffing marks are also visible on B3-1 on the edges of the pitting damage. This is classified as a secondary damage due to disturbance of the lubrication film in the vicinity of the pit, as well as due to an increase in contact pressure. Furthermore, a minor micropitting damage was observed on the tip of the TFF-affected B1-3 pinion tooth. In order to further examine the TFF damages on the B1-3 pinion and the B2-1 and B3-2 wheels, the damaged teeth were extracted and cut into sections.

4.2. *Fractographic analysis*

The fractographic analysis of the pinion-initiated TFF on B1-3, as well as the wheel-initiated TFF on B2-1 was conducted on a field emission scanning electron microscope (MIRA 3 XMU) equipped with electron backscatter diffraction (EBSD) and energy dispersive X-ray (EDS) detectors. A second wheel-initiated TFF on B3-2 was analyzed on a second field emission scanning electron microscope (TESCAN VEGA 4 LMU), similarly equipped with EBSD and

EDS. The wheel analysis did not reveal any insight into the cause of failure or its initiation depth, as excessive plastic deformation of the fracture surfaces removed all fatigue fracture features.

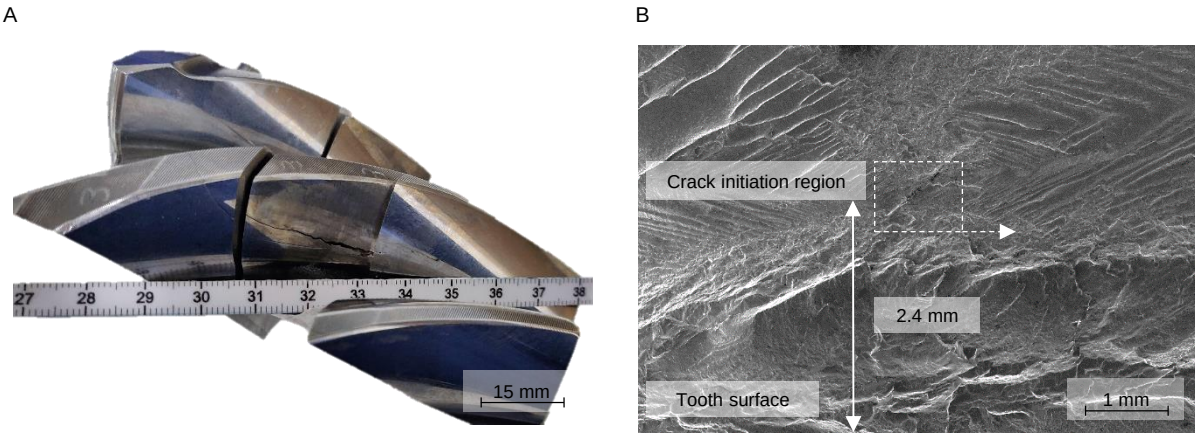

Fig. 11. TFF on pinion B1-3 with crack location and fracture surface extraction in (A) and SEM analysis showing a 1.4 mm long MgO-Al_2O_3 spinel in the crack initiation site

Fig. 11A visualizes the extraction of the analyzed pinion tooth section and the approximate position of the TFF on B1-3 mid flank and mid tooth height. The performed EDS analysis identified a 1.4 mm long MgO-Al_2O_3 spinel in a depth of 2.4 mm in the crack initiation site. The severely elongated spinel was orientated approximately in the pinion's forging direction and in a 45° angle to the load-carrying gear flank. Whereas Fig. 11B visualizes the general orientation of the inclusion on the fracture surface, Fig. 12A and B show the length of the inclusion through SEM and EBSD images.

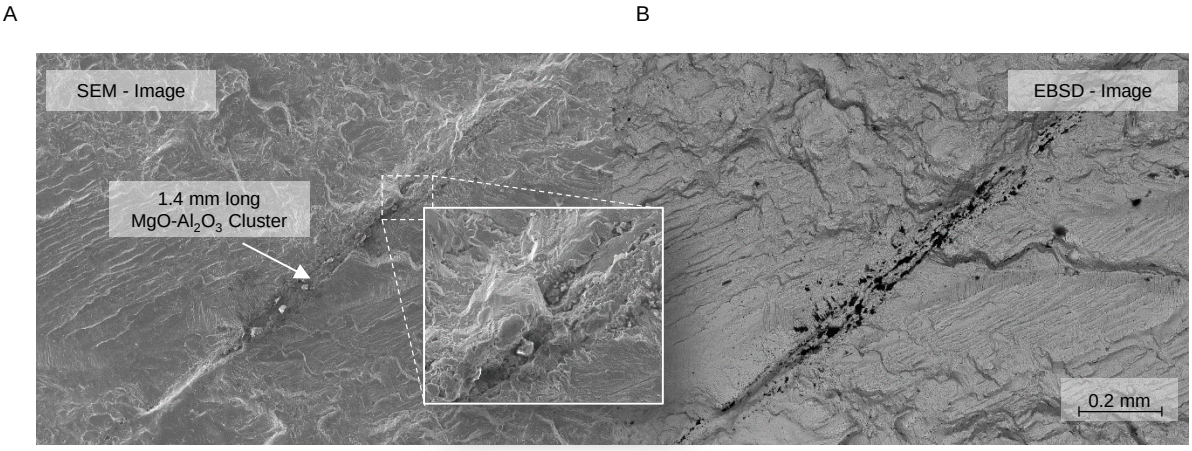

Fig. 12. Study of crack initiating $MgOAl_2O_3$ inclusion on pinion B1-3 through (A) SEM and (B) EBSD

The comparison between the inclusion size on the B1-3 test gear and the VHCF tested 18CrNiMo7-6 and 34CrNiMo6 steels [4] relies on Murakami's model and its √area parameter [11]. The √area parameter describes the square root of the projected area of an inclusion, perpendicular to the maximum principal stress. The maximum principle stress as a result of the Hertzian contact is perpendicular to the load carrying flank, whereas the studied inclusion is tilted in tooth width and profile direction. It is uncertain if the entire length of the identified inclusion should be considered in the calculation of the √area parameter. The average √area parameter found on VHCF fracture surfaces of the uniaxial fatigue specimen was 80 µm, compared to the 330 µm for the reported spinel on B1-3. According to Murakami, the large defect size is equivalent to a 20 % lower fatigue strength f_{-1} than outlined in

Eq. 2. The developed multiaxial fatigue criterion, strength and stress models suggest a large failure probability for B1-3 regardless of the identified inclusion. Either the orientation of the inclusion meant that only its cross-section was critical to the crack initiation or the developed methodology overestimates subsurface failures on pinion teeth. Currently, the same material model is implemented for pinions and wheels, depending only on the measured hardness profiles and not on the different blank sizes, forging methods and ratios.

The wheel-initiated TFF on B3-2 (shown in Fig. 13A) features a heavily deformed fracture surface with faint fatigue features like ratchets or river marks. A closer study of the assumed initiation region 4 mm below the surface did not reveal any significant non-metallic inclusions but rather a 0.6 mm long ridge, parallel to the tooth surface. With TFF cracks typically initiating parallel to the load-carrying flank under shear in mode II and propagating under bending in mode I, the identified ridge can be considered as a possible initiation site. The observed surface topography bears resemblance to the matrix initiated failures from large, soft austenite grains on the 34CrNiMo6 VHCF specimen [4] (see Fig. 13B). The predicted maximum utilization at 3.7 mm below the surface further supports the identified crack initiation site.

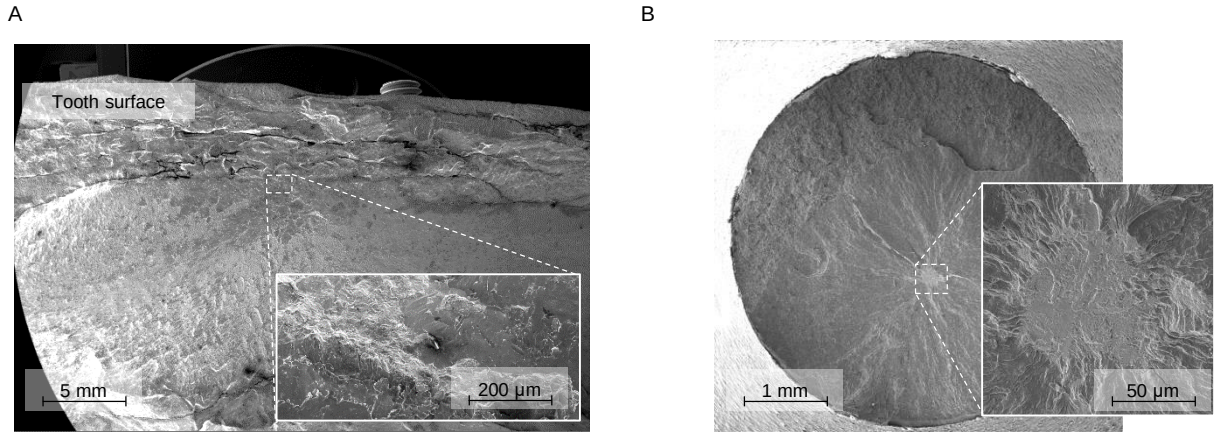

Fig. 13. TFF on wheel B3-2 with (A) fracture surface and a close-up of assumed initiation site compared against (B) crack initiation from large, retained austenite grain[4] in 34CrNiMo6 VHCF uniaxial fatigue specimen

5. Discussion

As shown through the performed gear endurance tests, the presented methodology, comprised of the strength, stress and fatigue models, can differentiate between and accurately predict pitting and TFF or subsurface fatigue damages. Of the studied gear sets, 6 TFF damages were recorded, of which 5 occurred on the tested wheels. The documentation and accurate modelling of the hardness differences between the studied pinions and wheels were essential in capturing the majority of wheel-initiated TFF damages [12]. The wheels were found to generally have a thinner *CHD* and steeper transition between the hard surface and soft core. As the hardening layer is furthermore used to approximate the initially compressive and subsequently tensile residual stresses, the differences between the tested pinions and wheels are further amplified. Pitting occurred on a single pinion tooth, approximately at half tooth height. The proposed strength and stress models, along with the BO multiaxial fatigue criterion, correctly identify the same location to be critical. In addition, large utilizations are predicted for the pinion dedendum, suggesting a substantial pitting or micropitting risk in this tooth segment. The fatigue model is also able to assess the likelihood of tooth root breakage. The analysis shows an approximately 1.6x higher risk for tooth root breakage on the tested pinions than wheels, compared to the 1.15x predicted by the LTCA and ISO [2, 14]. The further analysis and recalculation of gear studies focusing on tooth root breakage [28] is planned for the future to better assess the accuracy of the fatigue model in this respect.

The only pinion-initiated TFF featured a comparably large, elongated non-metallic inclusion in its crack initiation site, suggesting lower fatigue properties than currently implemented in the material model. A large material utilization is predicted regardless in the relevant material depth of 2.7 mm, suggesting that the fatigue model in its

current form potentially overestimates subsurface fatigue failures on pinion teeth. Further tests are necessary to quantify the subsurface fatigue differences between pinion and wheel teeth, which could be accounted for through a blank diameter or forging ratio based technological size factor.

A revised load cycle factor K_{NT} is proposed as a result of the performed gear tests. It relies in its approximation on the MLM [21] and considers failures (here pitting and TFF) alongside run-outs. In magnitude and shape, it is shown to be very comparable to the established tooth root and pitting lifetime factors [1, 2]. This study tested gears manufactured according to three different heat treatment protocols, making a stress-based prediction of the lifetime factor impossible. By relying on the calculated material utilization, an approach is presented that incorporates the gear size, the specific heat treatment protocol and the applied load. Consequently, other gear tests could be include and consider in the prediction of the proposed lifetime factor.
The study mentions the previously developed size factor K_X as a function of the gear's mean normal module m_{mn} [5], but utilizes the weakest link theory [22] to consider the volumetric differences between tested pinions and wheels. Due to the larger number of teeth, larger size factors were predicted for the wheels. In this study, the same size factor is applied throughout the gear tooth. However, as tooth root bending stresses act on a much smaller volume than subsurface stresses, the model might overestimate tooth root breakages in its current form.

As shown in the previous studies [5], the estimated material utilizations for different stress-based multiaxial fatigue criteria vary greatly throughout a gear's mean cross-section. Especially in the case of highly loaded gears, a reliable surface and subsurface fatigue prediction becomes difficult with established criteria. The BO criterion, along with the proposed stress and material models, are proven to be capable of differentiating between the major fatigue failure modes on bevel gears, i.e. pitting, tooth root breakage and TFF or subsurface fatigue. Although further stringent studies are necessary to prove the applicability of the developed model to other gear failures than TFF, it opens the door to a fatigue assessment of a gear design in a single calculation. Although this study focused on bevel gears, none of the implemented assumptions exclude an application to cylindrical gears. In fact, the 2D plane strain stress model utilized in this study should yield even more accurate results when applied to cylindrical gears.

The material model implemented in this study was developed for carburized CrNiMo steels and specifically large forgings of 18CrNiMo7-6 [4]. If data on the steel's average inclusion size and hardness profile are available, the presented methodology should be transferable to other case hardening steels (DIN EN 10084) that similarly underwent a heat treatment in a non-vacuum furnace.

6. Conclusion

The herein presented gear test results support the developed material, stress and fatigue models and demonstrate their applicability in predicting typical gear fatigue failure modes. Key findings of this study are:

(i) During testing, the majority of tooth flank fractures initiated on the wheels, despite the gear's 9:33 gear ratio. The larger material removal during final machining and the steeper case to core hardness transition on the studied wheels are believed to be major contributing factors.

(ii) A revised tooth flank fracture lifetime factor is proposed. It is based on the analysis of the calculated material utilization and incorporates thereby the studied gear size, produced hardness profile and occurring surface stresses. The consideration of other endurance tests of different gear sizes, geometries and hardness profiles is thereby enabled to improve upon the proposed lifetime factor.

(iii) A refined hardness, residual stress and material model is presented that accurately captures the subtle differences between the tested pinions and wheels. It improves upon the fatigue assessment and predicts the majority of wheel-initiated tooth flank fractures reliably.

(iv) This study, alongside the previous publications on subsurface fatigue, outline a methodology capable of predicting tooth flank fracture in bevel gears and possibly all typical gear fatigue failure modes in a single calculation framework.

Acknowledgement

The authors would like to thank Kongsberg Maritime Finland OY for supporting this research through the “High Torque Gears” project, the financing of the gear tests and for the possibility to analyze and publish the findings. Sincere gratitude is extended to ATA Gears Oy for the co-financing of the gear tests and the pre- and post-analysis of the gear specimens. In addition, the authors gratefully acknowledge the funding of this research project through the Norwegian Research Council (NFR) – Project ID 270828.

Data availability statement

The data used in this manuscript can be made available on request from the corresponding author.

References

[1] *ISO 10300-2:2014 - Calculation of load capacity of bevel gears - Part 2: Calculation of load capacity of bevel gears*, 2014.

[2] *ISO 10300-3:2014 - Calculation of load capacity of bevel gears - Part 3: Calculation of tooth root strength*, 2014.

[3] S. A. Böhme, D. Merson, and A. Vinogradov, "On subsurface initiated failures in marine bevel gears," *Engineering Failure Analysis,* vol. 110, p. 104415, 2020.

[4] S. A. Böhme, A. Vinogradov, H. Biermann, A. Weidner, A. Schmiedel, and S. Henkel, "Fatigue of carburised CrNiMo steel: Testing and modelling concept," *Fatigue & Fracture of Engineering Materials & Structures,* vol. 44, no. 3, pp. 788-804, 2020.

[5] S. A. Böhme, A. Vinogradov, J. Papuga, and F. Berto, "A novel predictive model for multiaxial fatigue in carburized bevel gears," *Fatigue & Fracture of Engineering Materials & Structures,* 2021.

[6] *DNVGL-CG-0036: Calculation of gear rating for marine transmissions*, 2015.

[7] J. Liu, Zenner, H., "Berechnung der Dauerschwingfestigkeit bei mehrachsiger Beanspruchung - Teil 1 und 2," *Materialwissenschaft und Werkstofftechnik* vol. 24, pp. 240-249 and 296-303, 1993.

[8] J. Papuga, L. Suchý, and M. Růžička, "Mean shear stress effect built into the multiaxial fatigue strength estimation method of an integral type," *MATEC Web of Conferences,* vol. 300, p. 16010, 2019.

[9] E. Cízová, "Parametry historie napetového tenzoru a jejich dopad na únavovou životnost," Master, Fakulta strojní Ústav mechaniky, biomechaniky a mechatroniky, Ceské vysoké ucení technické v Praze, 2021.

[10] FKM, *Rechnerischer Festigkeitsnachweis für Maschinenbauteile*. VDMA, 2012.

[11] Y. Murakami, *Metal Fatigue: Effects of Small Defects and Non-metallic Inclusions*. Cambridge: Academic Press, 2019.

[12] J. Thomas, "Flankentragfähigkeit und Laufverhalten von hart-feinbearbeiteten Kegelrädern," PhD, TU München, Munich, 1998.

[13] *ISO 6336-6:2016 - Calculation of load capacity of spur and helical gears - Part 6: Calculation of service life under variable load*, 2016.

[14] V. Baumann, G. Bär, A. Haase, B. Hutschreiter, and C. Hünecke, "Programm zur Berechnung der Zahnflanken – und Zahnfußbeanspruchung an Kegelrad – und Hypoidgetrieben," vol. Heft 548, ed. Frankfurt: Forschungsvereinigung Antriebstechnik e.V., 1998.

[15] M. Hombauer, *Bestimmung der Graufleckentragfähigkeit von Kegelrad- und Hypoidverzahnungen* (Forschungsvorhaben Nr. 516). Forschungsvereiningung Antriebstechnik e.V., 2013.

[16] M. Klein, *Bestimmung der Fresstragfähigkeit von Kegelrad- und Hypoidverzahnungen* (Forschungsvorhaben Nr. 519). Forschungsvereinigung Antriebstechnik e.V., 2013.

[17] L. Wech, "Untersuchungen zum Wirkungsgrad von Kegelrad- und Hypoidgetrieben," TU München, 1987.

[18] K. Varis, J. Rinnevalli, R. Vanninen, and J. Keski-Rahkonen, "Examination of the Crack Initiation and Propagation in a Spiral Bevel Gear," Stressfield for Rolls-Royce Marine, 2014.

[19] R. Weber, "Auslegungskonzept gegen Volumenversagen in einsatzgeharteten Stirnradern," PhD, Institut für Werkstofftechnik, Universität Kassel, 2015.

[20] O. R. Lang, "Berechnung und Auslegung induktiv randschichtgehärteter Bauteile," *Kloos, K. H. (Hrsg.); Grosch, J. (Hrsg.): Induktives Randschichthärten. Berichtsband, Tagung 23. bis 25. März 1988, München: Arbeitsgemeinschaft Wärmebehandlung und Werkstofftechnik (AWT),* pp. 332 - 348, 1989.

[21] F. Pascual, Meeker, W., "Analysis of fatigue data with run-outs based on a model with non constant standard deviation and a fatigue limit parameter," *Journal of Testing and Evaluation,* vol. 25, pp. 292-301, 1997.

[22] R. Rabb, *Todennäköisyysteoriaan pohjautuva väsymisanalyysi*. Norderstedt: Books on Demand, 2013.

[23] *ISO 6336-5:2016 - Calculation of load capacity of spur and helical gears - Part 5: Strength and quality of materials*, 2016.

[24] T. Reimann, *Untersuchungen zur erweiterten Quantifizierung der Tellerradgrübchentragfähigkeit bei Kegelrad- und Hypoidverzahnungen* (Forschungsvorhaben Nr. 748 I). Forschungsvereinigung Antriebstechnik e.V., 2020.

[25] I. Boiadjiev, J. Witzig, T. Tobie, and K. Stahl, "Tooth flank fracture – basic principles and calculation model for a subsurface initiated fatigue failure mode of case hardened gears," in *International Gear Conference 2014: 26th–28th August 2014, Lyon*Oxford: Chandos Publishing, 2014, pp. 670-680.

[26] M. Klein, J. Seabra, B. R. Höhn, K. Michaelis, and R. Annast, "Theoretical and experimental investigations about flank breakage in bevel gears," *Industrial Lubrication and Tribology,* vol. 63, no. 1, pp. 5-10, 2011.

[27] M. MackAldener, "Tooth Interior Fatigue Fracture & Robustness of Gears," PhD, Department of Machine Design, KTH - Stockholm, Stockholm, 2001.

[28] C. Wirth, *Entwicklung eines Berechnungsberfahrens zur Grübchen- und Zahnfußtragfähigkeit von Hypoidrädern* (Forschungsvorhaben Nr. 411). Forschungsvereinigung Antriebstechnik e.V., 2009.